PCCP

PAPER

View Article Online
View Journal | View Issue

Cite this: *Phys. Chem. Chem. Phys.*, 2015, **17**, 7775

Comparison of photocatalytic and transport properties of TiO_2 and ZnO nanostructures for solar-driven water splitting†

Simelys Hernández,*[ab] Diana Hidalgo,[ab] Adriano Sacco,[a] Angelica Chiodoni,[a] Andrea Lamberti,[ab] Valentina Cauda,[a] Elena Tresso[ab] and Guido Saracco[b]

Titanium dioxide (TiO_2) and zinc oxide (ZnO) nanostructures have been widely used as photo-catalysts due to their low-cost, high surface area, robustness, abundance and non-toxicity. In this work, four TiO_2 and ZnO-based nanostructures, *i.e.* TiO_2 nanoparticles (TiO_2 NPs), TiO_2 nanotubes (TiO_2 NTs), ZnO nanowires (ZnO NWs) and ZnO@TiO_2 core–shell structures, specifically prepared with a fixed thickness of about 1.5 μm, are compared for the solar-driven water splitting reaction, under AM1.5G simulated sunlight. Complete characterization of these photo-electrodes in their structural and photo-electrochemical properties was carried out. Both TiO_2 NPs and NTs showed photo-current saturation reaching 0.02 and 0.12 mA cm^{-2}, respectively, for potential values of about 0.3 and 0.6 V *vs.* RHE. In contrast, the ZnO NWs and the ZnO@TiO_2 core–shell samples evidence a linear increase of the photocurrent with the applied potential, reaching 0.45 and 0.63 mA cm^{-2} at 1.7 V *vs.* RHE, respectively. However, under concentrated light conditions, the TiO_2 NTs demonstrate a higher increase of the performance with respect to the ZnO@TiO_2 core–shells. Such material-dependent behaviours are discussed in relation with the different charge transport mechanisms and interfacial reaction kinetics, which were investigated through electrochemical impedance spectroscopy. The role of key parameters such as electronic properties, specific surface area and photo-catalytic activity in the performance of these materials is discussed. Moreover, proper optimization strategies are analysed in view of increasing the efficiency of the best performing TiO_2 and ZnO-based nanostructures, toward their practical application in a solar water splitting device.

Received 15th December 2014,
Accepted 11th February 2015

DOI: 10.1039/c4cp05857g

www.rsc.org/pccp

1. Introduction

With increasing concern over the fossil fuel depletion and the environmental degradation, energy is one of the greatest issues that humanity will be facing in the coming years. Hydrogen, present in the water molecules, is an efficient energy carrier and is also environmentally friendly: therefore using solar energy to split water into oxygen and hydrogen (also called "artificial photosynthesis") is a key point towards the development of sustainable and renewable energy devices.

More than 40 years after the pioneering work of Fujishima and Honda,[1] the search for suitable semiconductors to be employed for the water dissociation into molecular hydrogen and oxygen is still an open challenge. It has been found[2] that the photochemical water-splitting reaction can be catalyzed by over 140 metal oxides, perovskites and oxynitrides, and the principal controlling factors of the photocatalysis activity have been identified. Nevertheless many questions concerning the molecular mechanisms of water reduction and oxidation and the charge transfer dependence on the electronic and structural properties have not been completely solved yet, and the ideal semiconducting photocatalyst has still to be identified. At the same time, research efforts focused on proposing artificial photosynthesis devices have been recently greatly increased in number and importance, but functional prototypes with convenient efficiencies have still to be fabricated.[3]

The H_2 photocatalytic generation involves three main steps: (i) absorption of photons (with energy higher than the semiconductor band gap (E_g) and consequent generation of electron–hole (e^-–h^+) pairs in the semiconductor), (ii) excited charge carrier separation and migration within the semiconductor, and (iii) surface reaction of the carriers with water molecules. To provide the water splitting, the bottom of the semiconductor conduction band must be in a more negative energy position with respect to

---

[a] *Center for Space Human Robotics (IIT@POLITO), Istituto Italiano di Tecnologia, C.so Trento 21, 10129, Torino, Italy. E-mail: simelys.hernandez@polito.it; Tel: +39 0110904774/3418*
[b] *Department of Applied Science and Technology (DISAT), Politecnico di Torino, C.so Duca degli Abruzzi 24, 10129, Torino, Italy*

† Electronic supplementary information (ESI) available: (i) Long-time (12 h) *I–t* curves of both TiO_2 NTs and ZnO@TiO_2 photoelectrodes and (ii) FESEM images after PEC tests of the four studied materials. See DOI: 10.1039/c4cp05857g

the reduction potential of water to produce H_2; and the top of the valence band must be more positive than the oxidation potential of water to produce O_2. Furthermore, the photo-catalyst must be stable in aqueous solutions under photo-irradiation. The total amount of generated H_2 molecules is determined by the amount of excited electrons at the water/photo-catalyst interface capable of reducing water. Charge recombination and separation–migration processes are the two most important competitive processes that largely affect the efficiency of the photocatalytic reaction. Charge recombination reduces the number of e^-–h^+ pairs by emitting light or generating phonons. Efficient charge separation, fast charge carrier transport and limited bulk/surface charge recombination are thus fundamental characteristics of an optimal semiconductor photocatalyst material.

Since 1972,[1] titanium dioxide (TiO_2) has been the most commonly studied material for photocatalysis. It exhibits an appropriate band gap of about 3.2 eV, together with high photocatalytic efficiency, good chemical and optical stability, optimal environmental and biological compatibility.[4] Zinc oxide (ZnO) has also been largely considered because of its band gap energy, which is comparable to TiO_2,[5] with the energy levels located almost at the same positions, its higher electron mobility and lifetime,[6] relatively lower production costs and easy fabrication under a variety of nanostructures such as nanowires, nanoribbons, nanobelts, nanocombs, nanospheres, nanofibers, nanotetrapods.[7] To date TiO_2 and ZnO have been close to be ideal photocatalysts. They are relatively inexpensive and they provide photo-generated holes with high oxidizing power due to their wide band gap energy. Unfortunately their solar-to-hydrogen efficiency is limited by the high band gap and the many electron–hole recombination centers;[8] moreover, ZnO has the disadvantage of a facile dissolution under UV light irradiation in aqueous solution.[9]

Different routes have been adopted for enhancing the TiO_2 and ZnO photocatalytic performances. Based on the fact that size, shape and also defects significantly affect the final photocatalytic activity, the optimization of the morphology and the crystalline structure has been studied, and a large variety of micro and nanostructures has been suggested.[10] In particular, one-dimensional nanostructures such as nanorods, nanotubes and nanowires have emerged as a very promising alternative to nanoparticle-based architectures: the cylindrical and/or tubular configuration is very convenient to increase the surface area without affecting the total geometric surface and the unidirectional electric channel should allow a better charge transport.[11] Moreover, many strategies to change the chemical composition and surface properties of the semiconductor have been tried, for instance by ion implantation, doping, dye sensitization[12] or hydrogenation,[13] and also hybrid nanostructures, such as core–shell nanocomposites, have been proposed, which consist of an inner nanostructure encapsulated inside an outer shell of a different material.

In particular, our group has recently developed different easy and low-cost procedures for the synthesis of TiO_2 and ZnO-based nanostructures. In particular, TiO_2 anatase nanoparticles (TiO_2 NPs) leading to mesoporous films have been prepared through an innovative sol–gel method on Fluorinated Tin Oxide (FTO)-covered glasses.[14] Self-organized TiO_2 nanotubes (TiO_2 NTs) have been grown by anodic oxidation on Ti foils,[15,16] while ZnO nanowires (ZnO NWs) have been obtained on a FTO seeded substrate using a hydrothermal route.[17] Finally, ZnO@TiO_2 core–shell structures have been fabricated on FTO by covering the ZnO NWs with sol–gel synthesized TiO_2 nanoparticles.[18,19] In particular, the TiO_2 nanoparticle-based films, the ZnO nanowires and the ZnO@TiO_2 core–shell structures have already demonstrated promising photocatalytic properties for the water splitting reaction.[14,18] The ZnO@TiO_2 core–shell heterostructures offer some advantages: the TiO_2 shell functions as a protective layer to reduce the ZnO degradation and the multi-dimensional contact permits to fully utilize the heterojunction between the two semiconductors, which exhibits very favorable electron-transfer properties that are beneficial to an effective separation of the photogenerated e^-–h^+ pairs.[18,20,21] For what concerns the TiO_2 NTs fabricated in our laboratory, they are employed for the first time in this work for the solar water splitting reaction.

In general, due to the broad range of dimensions and thicknesses of fabricated TiO_2 and ZnO nanostructures, and because of the different testing operative conditions, a direct comparison of both transport properties and performance of photoactive electrodes, between our materials and those reported in the literature, is not straightforward. Thus, in this paper, the aim is to compare the transport and photo-catalytic properties of four different photoelectrodes based on TiO_2 and ZnO nanostructures, specifically prepared in order to have the same thickness and the same active area. The studied electrodes are based on (i) mesoporous films of TiO_2 NPs, (ii) TiO_2 NTs, (iii) ZnO NWs and (iv) 1D ZnO@TiO_2 core–shell nanostructures. The thickness of the four photoelectrodes has been fixed at about 1.5 μm and the active area to about 4 cm^2, in order to reliably compare the electronic and PEC properties of these materials under the same operative conditions, for the sunlight-activated water splitting reaction. The morphological and optical properties of these nanostructures are also presented and discussed.

The electrochemical impedance spectroscopy (EIS) has been chosen as the main characterization technique to investigate the different charge transport mechanisms and interfacial kinetics. The role of key parameters such as electronic properties, specific surface area and photo-catalytic activity in the performance of these nanostructures is finally analyzed. Insights into different optimization strategies that can open up the way to increase the effectiveness of each of the studied materials are summarized, in view of their practical application in a solar water splitting device.

2. Experimental

2.1. Synthesis of the nanostructures

2.1.1. TiO_2 nanoparticle film fabrication by sol–gel synthesis. Titanium(IV) isopropoxide (TTIP, 97%), glacial acetic acid (AcOH, 99.7%) and the surfactant Tween 20, all from Sigma Aldrich were used as purchased. Firstly, TTIP was hydrolyzed in glacial AcOH and then the Tween 20 was added under vigorous stirring. The mixture was added dropwise to the deionized water and the final solution was aged under continuous stirring for 48 h at ambient temperature. TTIP, glacial AcOH, Tween 20 and water were at fixed molar ratios 1 : 10 : 1 : 300. The obtained solution was treated in a rotary evaporator at 40 °C for 2 h under vacuum conditions. The final sol containing the TiO_2 nanoparticles, homogeneous and stable for weeks, has then been used for the preparation of the TiO_2 NPs film. The sol was deposited onto FTO-coated glass (7 Ω sq^{-1} from Solaronix) in an exposed area of 2 cm × 2 cm by the spin-coating technique using a two-step deposition program: (1) 500 rpm for 10 s followed by (2) 3000 rpm for 10 s. The deposited film was dried at 360 °C for 30 min before spin-coating every successive layer. A total of three deposited layers were reached. Finally, the film was annealed at 500 °C in air at a heating rate of 1 °C min^{-1}, followed by natural cooling to room temperature. Further details of the synthesis and characterization of these films are described in our previous paper.[14]

2.1.2. TiO_2 nanotube array fabrication by anodic oxidation. TiO_2 nanotube arrays were grown by a quick anodic oxidation of Ti foil (250 μm thick, 99.6%-purity, Goodfellow) in an electrolytic solution made of 0.5 wt% NH_4F (98%, Sigma Aldrich) and 2.5 wt% deionized water in ethylene glycol (99.5%, Sigma Aldrich). The Ti foils were manually cut into 2 cm × 4 cm pieces and carefully cleaned by ultra-sonication in acetone and subsequently in ethanol. A rapid etching in a HF (1 wt%) aqueous solution was performed in order to remove the native oxide on the commercial Ti foil and to obtain a fresh surface for NT growth. Afterwards the samples were masked with a polyimide-based tape (exposed area 2 cm × 2 cm) and used as an anode in a two-electrode electrochemical cell (a platinum foil was used as a counter electrode) under continuous stirring and under ambient conditions. Anodization was performed applying a 60 V potential for 5 min in order to obtain a NT carpet with thickness ranging between 1.5 and 1.9 μm. Finally, the TiO_2 NTs were annealed at 450 °C (30 min heating ramp, 30 min in temperature, cooling down in 2 h) to crystallize them into the anatase phase. More details of the process are given elsewhere.[15,16]

2.1.3. ZnO nanowires grown by hydrothermal synthesis. ZnO nanowires were obtained using a hydrothermal route with a conventional approach[17] using two steps: first the preparation of a ZnO seed-layer on the FTO glass substrates (with an exposed area of 2 cm × 2 cm), and second the NW growth. Briefly, the seeded substrates were obtained by dip coating (speed 375 mm min^{-1}) the FTO-covered glass in a 10 mM solution of zinc acetate (Sigma, purity 98%) in ethanol and then calcining them in air at 350 °C for 1 h (heating rate 5 °C min^{-1}). Afterwards, the ZnO NWs were grown by immersing the seeded substrates in a 100 mL water solution of zinc nitrate hexahydrate ($Zn(NO_3)_2\cdot 6H_2O$, 25 mM, 98%, Sigma-Aldrich), hexamethyleneteramine (HMT, 12.5 mM, Sigma-Aldrich), polyethyleneimine (PEI, 5 mM, average $M_w \approx 800$, Sigma-Aldrich) and ammonium hydroxide (NH_4OH, 28%, 320 mM, Sigma-Aldrich) for 2 h at 88 °C under stirring (300 rpm). The obtained ZnO NWs were then thermally treated in air at 500 °C for 1 h (heating rate 1 °C min^{-1}).

2.1.4. ZnO@TiO_2 core–shell heterostructures prepared by sol–gel impregnation. The ZnO@TiO_2 core–shell structures were obtained as previously reported[18,19] by immersing for 10 min the ZnO NWs grown on FTO glass substrates in a non-acid titania precursor solution constituted by 0.46 M titanium isopropoxide (TTIP, 97%, Sigma-Aldrich), 0.28 M acetylacetone (99%, Fisher Aldrich) and 0.92 M bi-distilled water (from a Direct-Q, Millipore system) in 5 mL of 1-butanol (anhydrous, 99.8%, Sigma-Aldrich) under stirring at room temperature. The sample was then dried in the horizontal position and thermally treated in air at 450 °C for 30 min (heating rate 1 °C min^{-1}) for the complete titania crystallization into the anatase phase.

2.2. Morphological and optical characterization

The morphology and the structural properties of the different nanostructures were investigated by means of Field Emission Scanning Electron Microscopy (FESEM) using either a ZEISS Auriga or a ZEISS Merlin, and by means of a FEI TECNAI F20ST Transmission Electron microscope (TEM) operating in Bright-Field (BF) and Scanning Transmission Electron Microscopy (STEM) modes. The instrument was also equipped with a High-Angle Annular Dark Field (HAADF) detector. The samples for TEM/STEM characterization were prepared by detaching the nanostructures from the substrate, dispersing them in ethanol employing an ultrasonic bath, and putting a drop of the dispersion on the top of a holey carbon copper grid. The mean geometrical sizes of the different nanostructures, obtained from FESEM images, have also been used to calculate the mean exposed surface area (SA). The UV-visible spectra were recorded on a Cary 5000 Scan UV-visible spectrophotometer, using a diffuse reflectance integrating sphere. All spectra were recorded in both Kubelka–Munk function $F(R)$ and total reflectance (%R) modes, and background subtracted.

2.3. Photo-electrochemical characterization

The PEC experiments were performed in a Teflon reactor equipped with a quartz window for frontal illumination. All the tests were carried out in a three electrode configuration using the TiO_2 NP film, TiO_2 NTs, ZnO NWs or ZnO@TiO_2 core–shell heterostructures as the working electrodes for the water photo-electrolysis reaction, a platinum wire as the counter electrode, and an Ag/AgCl (KCl 3 M) as the reference electrode, in a 0.1 M NaOH aqueous electrolyte (pH = 12.7). N_2 was bubbled through the electrolyte solution for 30 min before the tests. The electrochemical measurements were performed using a multi-channel VSP potentiostat/galvanostat (by BioLogic), with EC-Lab® software (version 10.1×) for data acquisition. The current–voltage (I–V) characteristic curves were recorded by means of Linear Sweep Voltammetry (LSV) at a scan rate of 10 mV s^{-1}, when a constant open circuit voltage was achieved, varying the applied potential from −0.9 V to 0.8 V *vs.* Ag/AgCl, in the dark and under AM1.5G simulated sunlight (using a 450 W Xe lamp by Newport with an AM1.5G filter and a water filter model 6123NS) using a power density of 100 mW cm^{-2} (including 3.7 mW cm^{-2} in the UV range: 280 to 400 nm). The irradiance was measured by means of a Delta Ohm Photo-radiometer model HD2102.1.

Chrono-amperometric (*I*–*t*) tests were carried out to examine the photo-response of the nanostructures over time at −0.1 V and 0.3 V *vs.* Ag/AgCl (0.86 and 1.26 V_{RHE}) under continuous ON–OFF light cycles, with the same illumination condition used for the LSV. Further LSV was recorded with the TiO_2 NTs and the ZnO@TiO_2 core–shells with a higher light intensity than in the previous tests, using 220 mW cm^{-2} (having an UV contribution of 14 mW cm^{-2}). The measured potentials *versus* the Ag/AgCl reference electrode were converted to the reversible hydrogen electrode (RHE) scale *via* the Nernst eqn (1):

$$E_{\mathrm{RHE}} = E_{\mathrm{Ag/AgCl}} + 0.059 \cdot \mathrm{pH} + E^{\circ}_{\mathrm{Ag/AgCl}} \qquad (1)$$

where E_{RHE} is the converted potential *vs.* RHE in *V vs.* RHE (V_{RHE}), $E_{\mathrm{Ag/AgCl}}$ is the experimental potential measured against the Ag/AgCl reference electrode in *V vs.* Ag/AgCl ($V_{\mathrm{Ag/AgCl}}$), and $E^{\circ}_{\mathrm{Ag/AgCl}}$ is the standard potential of Ag/AgCl (KCl 3 M) at 25 °C (*i.e.* 0.21 V). EIS curves were recorded using the same potentiostat described above, from 0.1 Hz to 100 kHz, with an AC amplitude of 25 mV, at different applied potentials from −0.5 to 0.5 V *vs.* Ag/AgCl, in the dark and under AM1.5G simulated solar light (100 mW cm^{-2}). EIS for Mott–Schottky plots was performed at a frequency of 5 kHz, with an AC amplitude of 20 mV, from −0.8 to 0.7 V *vs.* Ag/AgCl with a scan step of 0.1 V.

3. Results and discussion

3.1. Morphology and structure

The morphology and the crystalline structure of the TiO_2- and ZnO-based nanostructures here studied have already been described elsewhere.[14,15,18,19] Nonetheless, 45° tilted FESEM views of the TiO_2 NPs and of the different vertically aligned nanostructures prepared for the present work are reported in Fig. 1. All the four considered nanostructures have a comparable thickness of about 1.5 μm. Fig. 1a shows the TiO_2 NP film, which is uniform and continuous, characterized by nanoparticles with a size ranging between 7 and 13 nm, interconnected in a mesoporous network.[14] As shown in Fig. 1b, the TiO_2 NTs grown by anodic oxidation are vertically arranged with respect to the Ti foil. The TiO_2 NTs are closely packed, with an outer diameter (o.d.) in the range 100–130 nm and inner diameter (i.d.) around 70 nm.[15] The ZnO NWs, shown in Fig. 1c, are almost vertically aligned, with a diameter ranging between 100 and 200 nm. Finally, Fig. 1d put in evidence the good coverage of the ZnO NWs with the titania shell made of crystalline anatase nanoparticles.[18,19] The different nanostructures have also been investigated with the TEM technique, both in BF-TEM and in STEM modes, as shown in Fig. 2. In Fig. 2a, two BF-TEM images at different magnification show the TiO_2 nanoparticles in the anatase crystalline form, as put in evidence by the selected area electron diffraction (SAED) analysis (not reported here) and by the Fast Fourier Transform (FFT) in the inset. The size of the particles is in the range 10–20 nm, in agreement with the previously reported FESEM characterization. In Fig. 2b, the BF-TEM characterization of the TiO_2 NTs is reported with different magnifications. The lower magnification put in evidence the shape of the TiO_2 NTs, where the wall, with a thickness of about 25 nm, is clearly visible. The high-magnification images collected in two distinct regions of the NTs confirm the polycrystallinity of the TiO_2 NTs, which are constituted by the anatase phase.[15] Fig. 2c shows two ZnO NW BF-TEM images at two different magnifications, in which the good crystallinity and the preferential orientation along the (002) direction of the ZnO NWs are clearly seen,[18] as put in evidence by the FFT in the inset. For what concerns the ZnO@TiO_2 core–shell structures, the HAADF-STEM images at two different magnifications in Fig. 2d put in evidence the *Z*-contrast and the good coverage of the ZnO NWs (brighter color, a higher atomic number) with the titania shell (darker color, a lower atomic number) with an average thickness of about 20–50 nm, made of crystalline anatase nanoparticles.[18,19]

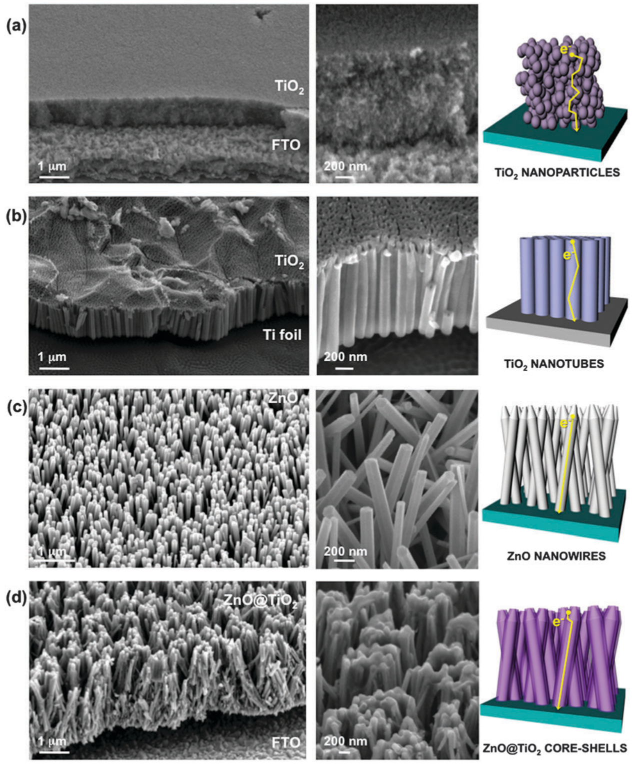

Fig. 1 45° tilted view FESEM characterization at two different magnifications and schematic representation indicating the e-flow path of the different nanostructures: (a) TiO_2 NPs, (b) TiO_2 NTs, (c) ZnO NWs and (d) ZnO@TiO_2 core–shells.

3.2. Optical properties

The UV-Vis spectra of the four studied TiO_2 and ZnO nanostructures, in Kubelka–Munk function *F*(*R*) and total reflectance (%*R*) modes are reported in Fig. 3a and b. As is well known, *F*(*R*) is directly proportional to the absorbance. In the range from 200 to 400 nm, F(R) is higher for the bare ZnO NWs than for the ZnO@TiO_2 core–shell sample and even for the pure titania nanomaterials, *i.e.* TiO_2 NTs and NPs film. Consistently, the spectra recorded in total reflectance mode (Fig. 3b) of both titania materials (NTs and NPs film) show a strong increase of the light

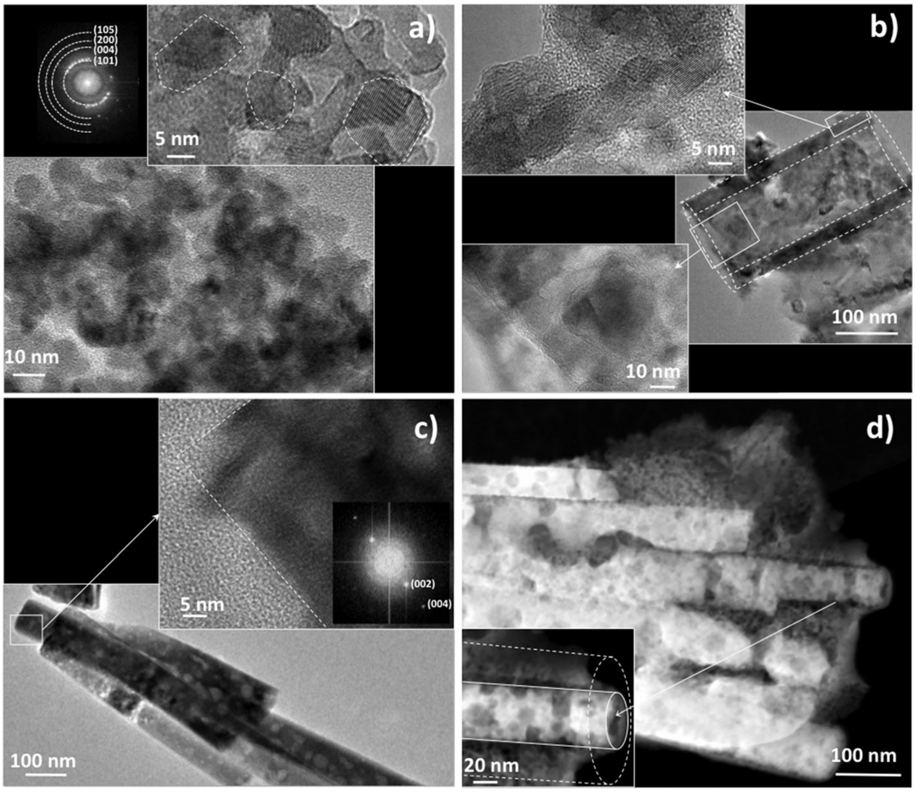

Fig. 2 TEM characterization of the different nanostructures. (a) BF-TEM images at two different magnifications of TiO_2 NPs; in the inset, the FFT of the high magnification image is reported. (b) BF-TEM of TiO_2 NTs at different magnifications. (c) Bright Field TEM of a group of ZnO NWs; in the inset, the FFT of the high-magnification image is reported. (d) HAADF-STEM of the ZnO@TiO_2 core shell: in the inset, a detail of the core–shell with a higher magnification is put in evidence.

scattering in the UV range (from 200 to 400 nm), whereas lower scattering is observed for the core–shell sample and is even lower for the bare ZnO NWs. This behavior is attributed to the high degree of crystallinity of the titania-based nanostructures and of the TiO_2 shell deposited on the ZnO NWs (consistent with the TEM and X-ray diffraction patterns reported elsewhere[18,19]), thanks to the thermal treatment at relatively high temperature (see the Experimental section for details). In addition, high scattering levels are expected for rough nanostructures with a high surface area. This is the case of the TiO_2 NP film,[14] the TiO_2 NTs[16] and of the core–shell structure[19] due to the titania nanoparticles that constitute the shell. The optical band gap values were estimated by using Tauc's method and are reported in the inset of Fig. 3b. The bare ZnO NWs show a higher E_g value (3.31 eV) than both the core–shell material (3.25 eV) and the nanostructured titania samples, *i.e.* TiO_2 NTs (3.27 eV) and TiO_2 NPs film (3.23 eV). The lower band gap values obtained for the core–shell, the TiO_2 NTs and TiO_2 NPs samples are attributed to the presence of anatase TiO_2, whose E_g has been reported to be about 3.2 eV[4]. Therefore, the narrowing of the E_g in the core–shell nanostructure with respect to the pure ZnO NWs is easily explained.[18]

3.3. Photo-electrochemical activity of the water splitting reaction

The PEC behavior of the TiO_2 NPs, TiO_2 NTs, ZnO NWs and the ZnO@TiO_2 core–shell heterostructures was evaluated using the prepared photoanodes, which have the same active area (4 cm^2), for the water photo-electrolysis reaction in 0.1 M NaOH solution (pH = 12.7). Fig. 4a reports the LSV behavior recorded with the four photoanodes. From the LSV scans under dark conditions, from 0.1 to 1.8 V_{RHE}, a tiny current in the range of 10^{-4} mA cm^{-2} was obtained for all the nanostructures until reaching the onset potential (E°) for the water oxidation reaction at about 1.75 V_{RHE}. As expected, the E° value is reached at potential higher than the theoretical one (E° = 1.23 V_{RHE}), due to the high overpotential effect of TiO_2 and ZnO semiconductors. In contrast, during the LSV under simulated sunlight irradiation (AM1.5G, 100 mW cm^{-2}), a sudden increase of the photocurrent is observed at potentials more negative than the redox potential E°, because part of the energy required for the oxidation is provided by the light. These results are in agreement with the behavior expected for a n-type semiconductor.[22]

Under sunlight illumination, the photocurrent density (J) of the TiO_2 NPs and TiO_2 NTs showed an important rise starting at about 0.17 and 0.19 V_{RHE}, respectively, reaching a maximum J value of 0.02 and 0.12 mA cm^{-2} at about 0.3 V_{RHE} and 0.6 V_{RHE}, respectively, which is associated with the saturation of the TiO_2 semiconductor.[14,23] In contrast, the ZnO NWs showed a pronounced increase of the photocurrent starting at about 0.40 V_{RHE}, which continues to rise until reaching a maximum J of 0.45 mA cm^{-2} at 1.7 V_{RHE}. The ZnO@TiO_2 core–shell electrodes showed similar behavior, but with an enhanced photo-response,

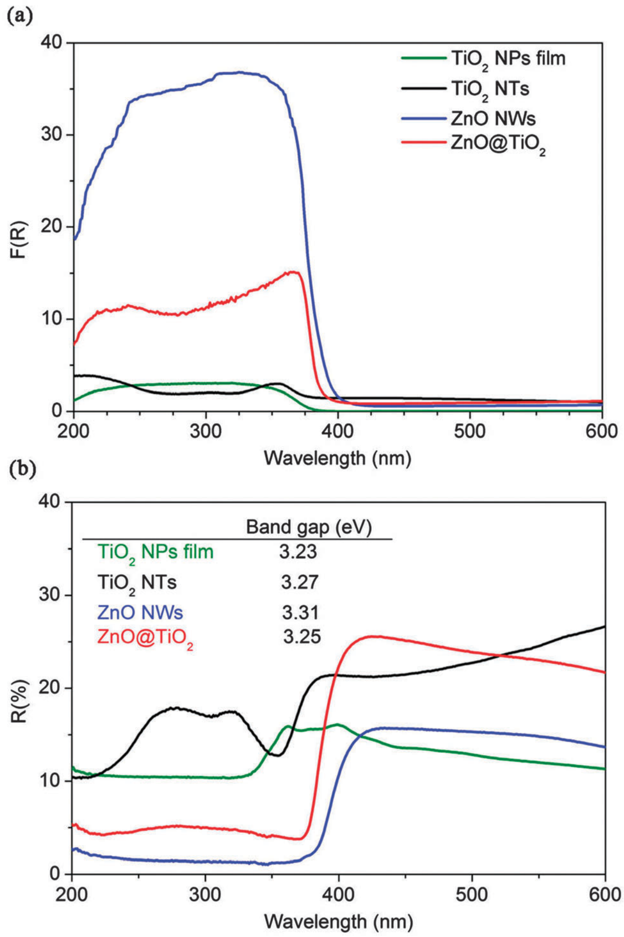

	Band gap (eV)
TiO_2 NPs film	3.23
TiO_2 NTs	3.27
ZnO NWs	3.31
ZnO@TiO_2	3.25

Fig. 3 Optical measurements: (a) Kubelka–Munk spectra, (b) total reflectance and the optical band gap for the samples: TiO_2 NP film (green line), TiO_2 NTs (black line), ZnO NWs (blue line) and ZnO@TiO_2 core–shell structures (red line).

reaching a maximum photocurrent density of 0.63 mA cm^{-2} at 1.7 V_{RHE}, a value that is about 1.5 times higher than the one obtained for the ZnO NWs. The larger photocurrents observed with the 1D-nanostructures (TiO_2 NTs, ZnO NWs and ZnO@TiO_2) with respect to the TiO_2 NPs film (even if they have a similar thickness) could be explained by a more efficient electron injection at the semiconductor–electrolyte interface and a faster electron transport from the photoanode to the substrate, which results in a higher number of collected photoelectrons.[18,19,24]

Additionally, it is worth noting that by coupling the ZnO NWs with a shell of TiO_2 NPs a significant increase of the photocurrent density during the water photo-electrolysis reaction is obtained. Indeed, this is related to the absence of a photocurrent saturation region, as occurs with TiO_2 NPs and TiO_2 NTs photoanodes upon illumination.[25] Therefore, these results are promising in comparison with other results reported in the literature for the water photo-electrolysis using TiO_2 and ZnO nanostructures.[25,26] For instance, a J value lower than 0.3 mA cm^{-2} at 1.8 V_{RHE} was reported by using nanocoral structures of ZnO[27] and N-doped ZnO NWs.[25] The photo-activity demonstrated by the ZnO@TiO_2 core–shell sample is also in-line with recent results on pure and N-doped rutile TiO_2 NWs (∼1.6 μm).[28] Even though, these values are still smaller than those recently

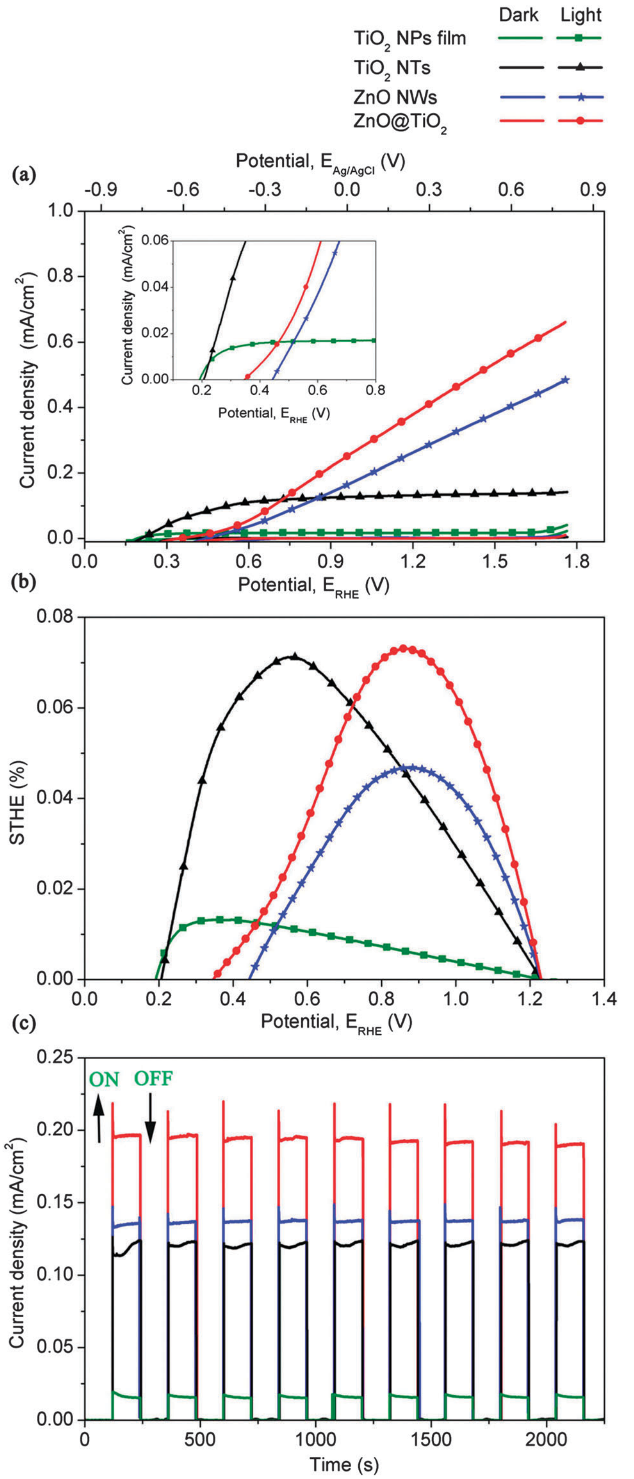

Fig. 4 Photoelectrochemical characterization of the samples: TiO_2 NP film (green line), TiO_2 NTs (black line), ZnO NWs (blue line) and ZnO@TiO_2 core–shell structures (red line). (a) LSV collected at a scan rate of 10 mV s^{-1} in the dark and under illumination (AM1.5G, 100 mW cm^{-2}); (b) Solar-to-hydrogen efficiency as a function of the applied potential; and (c) chrono-amperometric (I–t) curves at an applied potential of −0.1 V *vs.* Ag/AgCl under illumination with 120 s light ON–OFF cycles.

obtained by the coupling of ZnO with visible light absorbing semiconductors, *e.g.* ZnO–CdS core–shell NWs[29] and ZnO NWs sensitized with CdS/Se quantum dots.[30]

The solar-to-hydrogen efficiency (STHE) of each sample type under sunlight illumination was calculated from the *I–V* data according to expression:[31]

$$\mathrm{STHE} = J_i(1.23 - E_{\mathrm{RHE}})/I_{\mathrm{light}} \quad (2)$$

where J_i is the photocurrent density (mA cm^{-2}), E_{RHE} is the applied potential (V *vs.* RHE), and I_{light} is the irradiance intensity (*i.e.* 100 mW cm^{-2}).

The STHE curves in Fig. 4b show that the maximum of the curves for the four studied samples increases in the following order: TiO_2 NPs, ZnO NWs, TiO_2 NTs and ZnO@TiO_2, according to the following values: 0.013%, 0.047%, 0.071% and 0.073%, respectively. A significant increase of the STHE was obtained using the 1D-nanostructures with respect to TiO_2 NPs, due to their higher photocurrent densities.[18,19,24]

It is worth noting that both the TiO_2 NTs and the ZnO@TiO_2 samples gave similar maximum STHE but at different applied potentials, being lower for the NTs (*i.e.* 0.5 V_{RHE}) than for the core–shell sample (*i.e.* 0.9 V_{RHE}). This feature could likely be explained by the different photo-catalytic and transport properties of these two materials. In fact, the open circuit voltage (OCV), *i.e.* the voltage corresponding to $J = 0$, is an approximated measure of the flat band potential, which is an important parameter for semiconductor electrodes. Actually, this determines the band edge positions at the semiconductor–electrolyte interface, thus fixing the energies of conduction band electrons and valence band holes reacting with the electrolyte solution.[32] So, the shift of the OCV towards lower values is another indication of a better photocatalytic activity. The results in the inset of Fig. 4a indicate that both the TiO_2 NPs and the TiO_2 NTs samples have a lower flat band potential than the ZnO-based materials. Indeed, the TiO_2 NTs and NPs report almost the same OCV (about 0.20 V_{RHE}). Therefore, both the TiO_2 nanostructures present the onset E° at a lower value with respect to both the ZnO-based materials, as well as the coating of the ZnO NWs with the TiO_2 anatase shell results in an improved photocatalytic performance compared to the bare ZnO NWs. In fact, the increased photocurrent density of the ZnO@TiO_2 sample is reflected by both its higher STHE with respect to the ZnO NWs and the left-shift in the OCV, from 0.45 V_{RHE} (for ZnO NWs) to 0.34 V_{RHE} (for core–shell sample). The origin of this effect can rely on different reasons. First, well crystallized TiO_2 nanoparticles on the TiO_2 NPs, TiO_2 NTs or deposited on the surface of the ZnO NWs (in the core–shell sample) could effectively diminish the surface recombination sites, thus increasing the recombination resistance between electrons in the photoanode and holes in the electrolyte, leading to longer charge life-time.[20,33] On the other hand, electron transport within single crystalline ZnO NWs in the core–shell sample must be faster than in the pure NWs, due to a better charge separation induced by the formation of a heterojunction at the interface between the well crystallized ZnO and TiO_2 materials,[20] which was confirmed by TEM and diffuse reflectance analysis (explained above).

In order to investigate the photo-corrosion properties of the TiO_2 and ZnO nanostructures, the stability of the photoanodes was investigated as a function of time. Fig. 4c shows the *I–t* curves of all samples working at −0.1 V *vs.* Ag/AgCl (0.86 V_{RHE}). This potential was chosen since it is a representative value after the photocurrent saturation for both the TiO_2 nanostructures and is, as well, the potential of the maximum STHE for the ZnO NWs and ZnO@TiO_2 samples. The maximum photocurrent densities reached at this potential for all the samples increase in the order: TiO_2 NPs, TiO_2 NTs, ZnO NWs and ZnO@TiO_2, according to the following values: 0.016, 0.12, 0.14 and 0.19 mA cm^{-2}, respectively, which are in agreement with the *J* values reported in the LSV (see Fig. 4a). The same trend was also found at higher potentials. Moreover, a good photo-current stability was observed for all the four samples under numerous light ON–OFF cycles over a time of 38 min. Additionally, TiO_2 NTs and ZnO@TiO_2 (the most performing samples) were subjected to long term *I–t* curves (12 h at 0.3 V *vs.* Ag/AgCl) under 1 sun AM1.5G illumination, after which they showed a reduction in the activity lower than 20% (see ESI,† Fig. S1). Furthermore, the FESEM analysis performed after the PEC tests (see ESI,† Fig. S2) did not show a significant photo-degradation of TiO_2-based nanostructures. This result suggests that at least a part of the decrease in the photocurrent, in such a long time chrono-amperometry measurement, under liquid batch conditions, could be due to mass-transport limitations caused by either O_2 bubble formation or concentration gradients generated at the electrode surface, which can hinder the photo-activity of materials.[34] For more conclusive durability tests of the photoelectrodes, further tests should be subsequently made under continuous flow conditions in a different kind of electrochemical setup (see for instance the device reported in ref. 35). In contrast to the TiO_2-based electrodes, an initial stage of photo-corrosion was observed for the pristine ZnO NWs (see ESI,† Fig. S2). This fact confirms the low photo-corrosion resistance of the ZnO directly exposed to the NaOH electrolyte.[19]

It is important to point out that for a feasible application of a water photo-electrolysis device, the anodic photo-electrodes should present: (i) a high UV-Vis light absorption, (ii) a reduced overpotential for the water oxidation reaction, and (iii) efficient charge transport properties to be able to sustain high photocurrent densities. If these conditions are satisfied, the photoelectrodes would be able to reach STHE values of 10–15% with the minimum applied bias.[36] The best performing materials studied here, the TiO_2 NTs and the ZnO@TiO_2 core–shell samples, have different advantages and constraints that must be taken into consideration. With this aim, the relationship between the transport and the photo-catalytic properties of the studied nanostructures, and in particular of the TiO_2 NTs and of the ZnO@TiO_2 core–shell materials, is deeper investigated and discussed in the following sections.

3.4. Electrochemical impedance spectroscopy analysis

In order to better understand which is the most important process responsible for the different performances of the four

TiO_2 and ZnO investigated nanostructures, the PEC behavior of the studied photo-electrodes has been investigated using the EIS technique. The results of the EIS measurements performed at 1.23 V_{RHE} are reported in Fig. 5. In accordance with the LSV curves, the impedance modulus of both the TiO_2 photoelectrodes is larger than the ZnO-based ones (see Fig. 5a). Concerning the phase spectra, two features can be recognized, related to the two different processes occurring in the analyzed systems: a high frequency peak, associated with the charge transport properties of the photoelectrode material, and a low frequency peak associated with the charge transfer at the photoelectrode/electrolyte interface.[14] For the TiO_2-based and pure ZnO NWs photoanodes the two processes partially overlap, thus resulting in the formation of a one broad peak; on the other hand, the core–shell sample exhibits two well-distinguished peaks, one centered at about 4 Hz and the other one at about 200 Hz. In order to evaluate the time constants associated with the different processes for all the analyzed samples, the EIS data were modeled through the equivalent circuit shown in Fig. 5b[14] composed of: a series resistance R_s (accounting for the resistances of the conductive substrate, of the external electrical contacts and of the liquid electrolyte), a parallel between the resistance R_H and the capacitance C_H at the Helmholtz double layer (related to the low frequency process), and a parallel between the resistance R_{dl} and the capacitance C_{dl} in the depletion layer in the semiconductor (related to the high frequency process). For all the samples, the computed curves match well with the experimental data, as is evident in Fig. 5. Starting from the fitting parameters, the time constants τ_H and τ_{dl}, related to the charge transfer at the semiconductor/electrolyte interphase and to the charge transport in the semiconductor, respectively, were calculated through the following equations and their values are summarized in Table 1.

$$\tau_H = R_H C_H \tag{3}$$

$$\tau_{dl} = R_{dl} C_{dl} \tag{4}$$

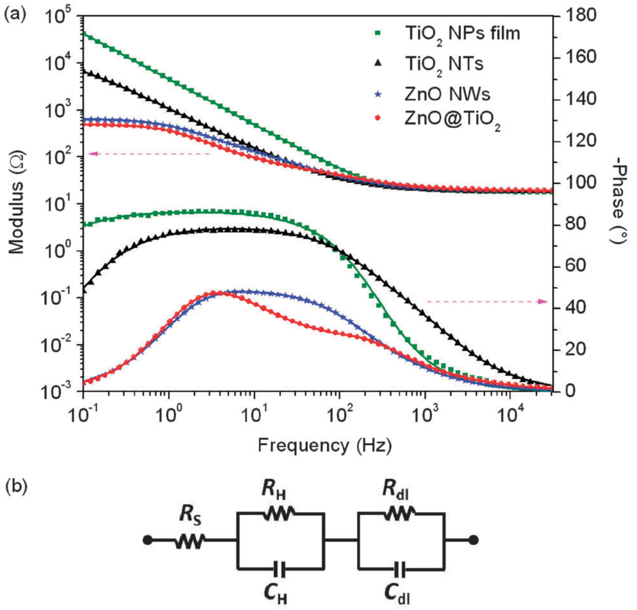

Fig. 5 (a) Bode plots of modulus (left axis) and phase (right axis) of the impedance of TiO_2 NPs, TiO_2 NTs, ZnO NWs and the ZnO@TiO_2 core–shell heterostructures acquired at an applied potential of 0.3 $V_{Ag/AgCl}$ (1.23 V_{RHE}) under illumination. The points represent the experimental data while the solid lines are the fitting curves. (b) Equivalent circuit used to fit the EIS data.

Table 1 Time constants related to the charge transfer processes involved in the water splitting reaction on the different TiO_2 and ZnO studied nanostructures, evaluated through EIS analysis at 1.23 V_{RHE}, under AM1.5G simulated sunlight (100 mW cm^{-2})

Sample	Exposed surface area, SA (cm^2)	R_s (Ω)	τ_H (s)	τ_{dl} (ms)
TiO_2 NPs	1500	17.92	10.75	333
TiO_2 NTs	600	2.78	2.530	76.0
ZnO NWs	100	19.25	0.150	16.0
ZnO@TiO_2	110	19.09	0.130	3.00

Moreover, with the aim of evaluating the influence of the surface area on the photo-electrochemical properties of the materials, the exposed surface area (SA) of the nanostructures (calculated by considering the dimensions measured through FESEM images) is also reported in Table 1.

By looking at the calculated parameters, as expected, the R_s value obtained for the TiO_2 NT sample is one-order of magnitude lower than R_s obtained for the other samples, due to the higher conductivity of the Ti foil substrate with respect to the FTO film. Moreover, the TiO_2 NP film is characterized by slower processes, when compared to the other nanostructures. In particular, it exhibits time constants which are 4 times larger with respect to the NTs-based photoelectrode, although the TiO_2 NPs SA is about 2.5 times higher than the one of the NTs. Regarding the τ_{dl} values, this difference can be attributed to the faster electronic transport inside the 1D nanostructure, when compared to the charge transfer by hopping among the nanoparticles.[16] Therefore, even if the photo-catalytic activity of the anatase crystalline phase found in both TiO_2-based materials should be similar (*i.e.* both these materials have a similar flat-band, as previously discussed), the transfer of charges at the TiO_2-electrolyte interphase is fastened due to the lower accumulation of charges in the NTs than in the NP nanostructure. As a consequence, the recombination of e^-–h^+ pairs is reduced, with a resulting increase in the kinetics of the water oxidation reaction in the NTs with respect to the NP sample, which is observed through the fastening of the charge-transfer at the semiconductor–electrolyte interphase (*i.e.* τ_H value). This hence explains the higher saturation photo-current evidenced with the TiO_2 NTs in comparison with the NP film (shown in Fig. 4a). In addition, as expected, the charge transport inside the ZnO NWs results even faster with respect to the polycrystalline TiO_2 NP and NT samples, the NWs being characterized by a monocrystalline structure.[37] Finally, the core–shell sample exhibited a five-times lower τ_{dl} value when compared to the bare nanowires. This feature can be explained by both the improvement in the electronic transport and in the efficient separation of charge-carriers at the ZnO@TiO_2 interphase[18] induced by the double annealing process performed in the heterostructure sample, which enhances the crystalline quality and favors the interconnection between the TiO_2 nanoparticles in the shell and the ZnO core.

3.5. Electronic properties *vs.* PEC behavior of TiO_2 NTs and ZnO@TiO_2 core–shells

Even if the core–shell material is characterized by better transport properties than the TiO_2 NTs, the latter demonstrated to achieve a STHE similar to the first one at a lower potential (see Section 3.3.). In order to analyze the reason for such a feature, the EIS measurements on these two materials were conducted in all the range of studied potentials, under sunlight illumination, and the results are reported in Fig. 6.

Both the materials evidenced almost constant charge transport parameters (*i.e.* R_{dl} and C_{dl}) after 0.6 V_{RHE}, indicating a quasi-conductive behavior of both the semiconductors under the electric field induced by the applied bias potential. In all the range of studied potentials, it is moreover confirmed the faster electron transport (lower τ_{dl}) within the ZnO@TiO_2 core–shells than in the TiO_2 NTs.

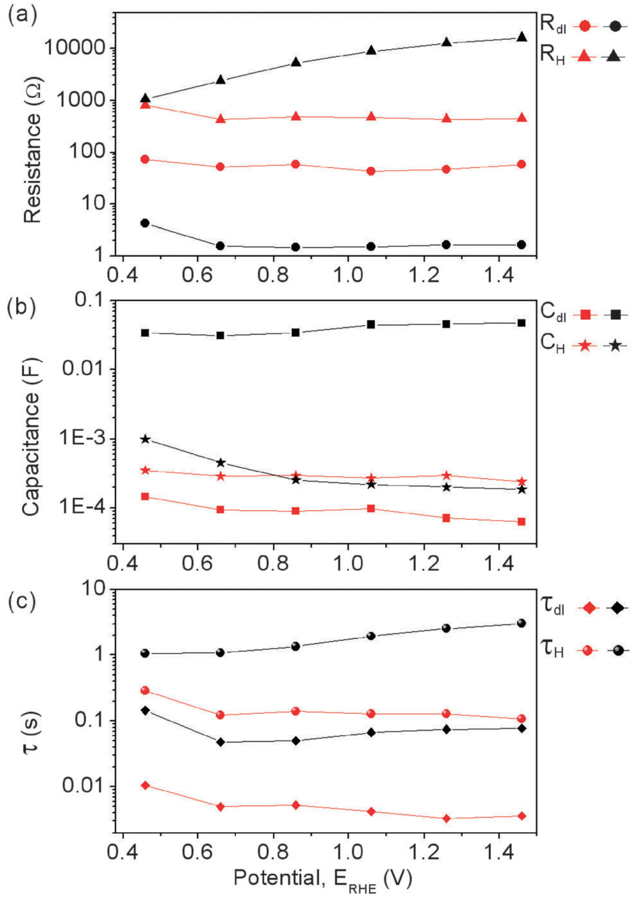

Fig. 6 Transport parameters from the fitting of EIS data obtained with the TiO_2 NTs (black points) and the ZnO@TiO_2 core–shell (red points) at different potentials under sunlight illumination: (a) resistance, (b) capacitance and (c) time constants.

On the other hand, in contrast with the core–shell material in which both the charge transfer parameters R_H and C_H remain constant after 0.6 V_{RHE}, in the TiO_2 NTs the R_H increases and the C_H slightly decreases with the potential. Since the capacitance at the Helmholtz double layer is related to the reaction rate at the surface of the photo-catalyst under illumination, C_H decreasing after 0.5 V_{RHE} must be correlated with the achievement of the maximum STHE at such a potential for the TiO_2 NTs. In addition, the charge-transfer resistance (R_H) of the NTs increases with the potential, leading to a simultaneous increase of the charge-carrier recombination at the surface of the TiO_2 photo-catalyst, due to the reduction of the e^-–h^+ separation efficiency.[38] In fact, this can explain the saturation of the photocurrent often observed with pure TiO_2 materials.[23] As a consequence of this and of the polycrystalline nature of the TiO_2 NTs, even if their exposed SA is six times higher than the one of the ZnO@TiO_2 sample, the τ_H (which is correlated with the reaction kinetics) remains 10-fold larger in the NTs than in the core–shells for all the range of applied potentials.

These findings evidence that not always the benefits of material nanostructuration could outweigh the disadvantages. The advantages are the high surface area and absorption volume close to the semiconductor–electrolyte interface, allowing the effective collection and reaction of photo-generated holes. The disadvantages are the partial loss of the electric field for charge separation and the increased opportunity for electrons to recombine with species at the electrode surface or in the electrolyte before being collected at the conductive substrate.[39] For such a reason, the other two major factors that can affect photocurrent efficiency of the nanostructured electrodes must be properly tuned: (i) the band gap energy, and (ii) the density of surface states and defects.

Regarding the first factor, the TiO_2 NTs have a slightly higher band gap (3.27 eV) than the ZnO@TiO_2 sample (3.25 eV), and thus the core–shell ability to exploit the visible component of sunlight illumination is slightly better than for the NTs. However, when these materials are illuminated in the UV-Vis range with the doubled of the intensity previously used (about 220 mW cm^{-2}), the *J* value at 1.23 V_{RHE} is increased 5 times with the NTs and only 2.4 times with the core–shells (as observed by comparing Fig. 4a and 7a). In addition, it is interesting to notice that under such conditions the maximum STHE are proportionally enhanced in both the materials, but with a different factor: 2.4 times for the NTs and only 1.2 times for the core–shell. These results could be justified by the higher IPCE of the NTs under UV illumination (maximum of 85%) than for the core–shell sample (maximum of 50%) at 1.23 V_{RHE} (data not shown): in fact, in the tests reported in Fig. 7a the UV component is about 4 times larger than in the previous ones (Fig. 4a). Moreover, these results are in agreement with the recent work of Qorbani *et al.*,[40] in which TiO_2 NTs were tested with different intensities of simulated sunlight up to 600 mW cm^{-2} and yielded a linear dependency between the generated photocurrent density and the applied illumination intensity, suggesting that the charge-carrier (e^-–h^+ pair) generation rate is the limiting step for the PEC water splitting.

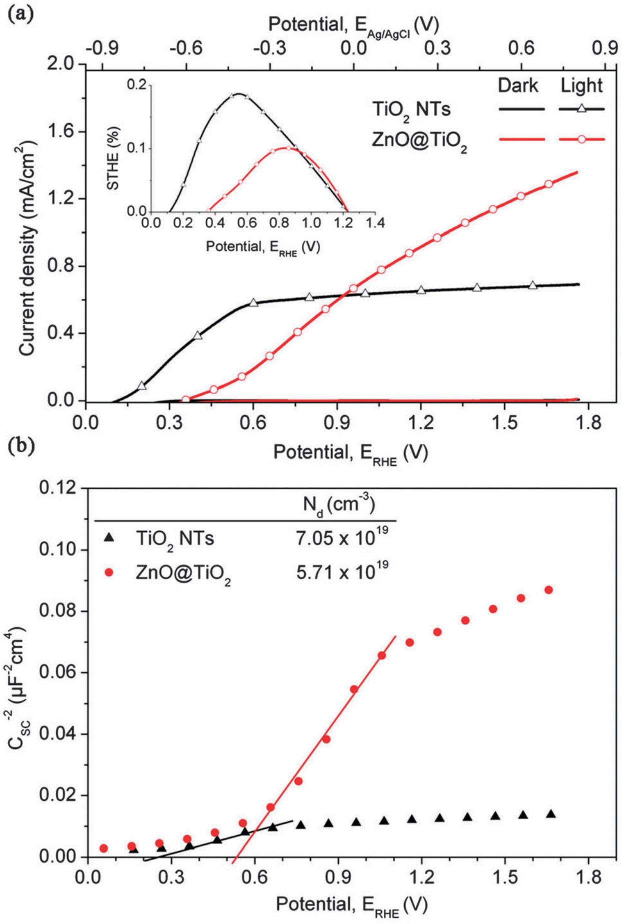

Fig. 7 (a) LSV in the dark and under UV-Vis illumination (intensity of 220 mW cm^{-2}), inset: STHE calculated from the data in (a). (b) Mott–Schottky plots of TiO_2 NTs (black triangles) and $ZnO@TiO_2$ core–shell structures (red circles).

Regarding the second factor, the charge carrier density was calculated according to the Mott–Schottky equation,[32] in order to evaluate the surface properties of these two nanostructures:

$$\frac{1}{{C_{\mathrm{SC}}}^2} = \frac{2}{e \cdot \varepsilon \cdot \varepsilon_0 \cdot N_{\mathrm{d}}}\left(E - E_{\mathrm{FB}} - \frac{kT}{e}\right) \tag{5}$$

where C_{SC} is the capacitance of the space charge region, ε_0 is the permittivity of the free space, ε is the dielectric constant of the semiconductor (100 for TiO_2 and 19 for the core–shell sample, calculated as a weighted volume value between ε of both ZnO and TiO_2), N_{d} is the donor density, e is the electron charge value, E is the applied potential, E_{FB} is the flat band potential and kT/e is the temperature dependent correction term (25 mV at room temperature).

The N_{d} values obtained from the linear fitting process are 7.05×10^{19} cm^{-3} for the TiO_2 NTs and 5.71×10^{19} cm^{-3} for the core–shells (see Fig. 7b), which are comparable with those usually observed for ZnO NWs and TiO_2 NTs.[23,41] The materials have similar N_{d}; however, if these values are normalized by the SA, it results that the core–shells (5.19×10^{17}) have a higher donor density per unit of active surface with respect to the TiO_2 NTs (1.18×10^{17}). A higher N_{d} can also shift the Fermi level of semiconductors toward its conduction band, which further facilitates the charge separation at the semiconductor/electrolyte interface. Thus, this enhanced charge separation and the most favorable charge transport are the most probable reasons for the higher photocurrent values reached with the core–shell samples at high potentials (>0.9 V_{RHE}) than the ones obtained with the pure TiO_2 nanostructure with the saturation of the photo-current.

These results, together with the ones reported in the Sections 3.3. and 3.4., evidence the promising photo-electrochemical ability of both the TiO_2 NTs and $ZnO@TiO_2$ core–shell nanostructures. In addition, they indicate that different possible strategies for optimizing the solar-induced water splitting activity of these nanostructured photoelectrodes can be suggested. In particular:

– The main advantage of the TiO_2 NTs is the low flat-band potential, which allows obtaining high photo-currents with a reduced bias. This intrinsic property of the TiO_2 NTs contributes in obtaining high STHE with a low consumption of extra energy in the PEC water splitting system. The deposition of a co-catalyst could be for example a key solution to improve the charge-carrier separation at the TiO_2 NTs-electrolyte interphase, which has been identified from our results to be the factor limiting their photocurrent. For example, the deposition of Pt nanoparticles in the top and walls of 10 μm-long TiO_2 nanotube arrays made by Lai *et al.*[42] yielded an enhancement of J from 16.3 to 24.2 mA cm^{-2} in 2 M Na_2CO_3–ethylene glycol solution with 320 mW cm^{-2} of simulated sunlight illumination. However, there are a few examples in which low-cost and earth-abundant catalysts (*e.g.* Co-, Mn- or Cu-based materials) have been deposited on TiO_2 NTs.[43] Similarly, the deposition of a co-catalyst in the high available surface of the TiO_2 in the shell of the $ZnO@TiO_2$ electrode can be exploited to reduce its onset potential.

– Both the TiO_2 NTs and the core–shells can be prepared having different sizes and lengths with a low-cost process and in a few synthesis steps. However, there are a few examples in the literature of $ZnO@TiO_2$ electrodes prepared and tested for the PEC water oxidation[18,44] and the ZnO NW length is often <2 μm. In contrast, the anodic oxidation process commonly used for the synthesis of the NTs renders easy the increase in their length and, thus, the enhancement of the active surface available for the reaction. It is important to point out that the results here reported with the $ZnO@TiO_2$ ($J < 0.7$ mA cm^{-2}) are in-line with or even more performing than some literature values obtained for both pure and doped ZnO NWs[45] and for 1D TiO_2–ZnO nanostructures[26] tested under AM1.5G sunlight. Even though, good performances have also been reached with other TiO_2-based nanostructures: *e.g.* Pan *et al.* reported 2 mA cm^{-2} obtained with a 2–4 μm-long hierarchical TiO_2 nanobelt–ZnO nanorod in 0.5 M Na_2SO_4 (120 mW cm^{-2}) and Wang *et al.*[31] obtained ~2.8 mA cm^{-2} with H_2-treated rutile TiO_2 NWs (2–3 μm length). The latter was the most performing value reached with TiO_2 NWs. Instead, TiO_2 nanotube arrays with a length ranging from hundreds of nm up to 45 μm, with different aspect-ratios, were reported with even better results for the water photo-electrolysis.[46–48] For instance, Sun *et al.*[46] reached 5 mA cm^{-2} in KOH (110 mW cm^{-2}) with TiO_2 NTs with an optimized length of 7 μm, made in 1 h of electrochemical anodization; Gong *et al.*[47] prepared highly ordered TiO_2 nanotube arrays by a three-step electrochemical anodization process with a length up to 18 μm (i.d. 50 nm), and reached a maximum J of about 24 mA cm^{-2} with the 1.2 μm-long sample in 0.5 M KOH.

– The photo-catalytic properties of both the TiO_2 NTs and the ZnO@TiO_2 can be further enhanced by modifying their optical or surface properties.[49] In this regard, one approach that has been often used is the doping (*e.g.* with C, N, S *etc.*) or the creation of bilayered systems with low band-gap semiconductors (*e.g.* WO_3, CdSe, CdS, *etc.*),[49,50] in order to enhance visible light absorption, charge separation and charge transport. Good examples are the C-doped TiO_2 NTs prepared by Park *et al.*[51] (~2 μm length, i.d. 70 nm) obtaining a J value close to 1 mA cm^{-2}, or the $TiO_{2-x}C_x$ nanotubes annealed in a H_2 atmosphere by Mohapatra *et al.*[52] reaching about 3 mA cm^{-2}, both under sunlight conditions in a 1 M KOH electrolyte. Nonetheless, really impressive results were recently reported by combining the use of heterostructures with a high visible light absorber and concentrated sunlight. For instance, Qorbani *et al.*[40] made CdS-sensitized TiO_2 NTs (2.9 μm length, 125 nm i.d.) yielding up to 28 mA cm^{-2} with an illumination of 4 suns (400 mW cm^{-2}), and Li *et al.*[53] prepared ZnO/CuS and ZnO/$CuInS_2$ core/shell nanorod arrays producing about 8 and 16.9 mA cm^{-2}, respectively, by using 5 suns of incident light and the Na_2S electrolyte.

– As shown in Fig. 7a and as discussed above, the illumination with concentrated light is an operative condition that could really mark the difference for the performance of a TiO_2 or ZnO-based device, due not only to the high amount of photo-generated holes that can enhance the inherent activity of these materials, but also to the low-cost availability of solutions to produce concentrated light (*i.e.* through the use of a polymeric Fresnel lens).

4. Conclusions

Four TiO_2 and ZnO-based nanostructures, having the same active area and similar thicknesses, were deeply characterized and compared in terms of their structural and photoelectrochemical properties. FESEM and TEM analysis evidenced the structural differences and the high degree of crystallinity of the various materials. Optical measurements allowed us to evaluate the energy gap values and to appreciate the occurrence of scattering effects due to the high surface area of the different structures coupled with their characteristic dimensions. Photoelectrochemical activity measurements and electrochemical impedance spectroscopy analysis showed an improvement in charge collection efficiency of 1D-nanostructures, related to a more efficient electron transport in the materials. The highest photocurrent density and photo-conversion efficiency in our system were obtained with the ZnO@TiO_2 core–shells and with the TiO_2 NTs. The core–shell heterostructure reached up to 0.63 mA cm^{-2} at 1.7 V_{RHE} and had a maximum STHE of 0.073% (at 0.9 V_{RHE}) under sunlight illumination of AM1.5G (100 mW cm^{-2}), this being the best performance ever reported for ZnO@TiO_2 for this application. In addition, the TiO_2 NTs attained a saturation photocurrent of 0.12 mA cm^{-2} from about 0.5 V_{RHE}, potential at which a maximum STHE of 0.071% yielded, similar to what obtained with the core–shell sample under the same operative conditions but at a lower applied bias. EIS analysis evidenced that the TiO_2 NPs exhibited time constants 4 times higher with respect to the NTs-based photoelectrode, which justifies the worst performance of the 3D NP nanostructure with respect to the 1D TiO_2 NTs. Moreover, the increase of the charge-carrier recombination at the TiO_2–electrolyte interface in the TiO_2 NTs with the applied potential indicated a reduction of the e^-–h^+ separation efficiency in this polycrystalline material, explaining the reason for the photocurrent saturation. Therefore, the charge transfer time constant obtained for the TiO_2 NTs was 10-fold higher than in the core–shells, for all the range of applied potentials: this occurrence was identified to be mainly responsible for the lower photocurrents of the TiO_2 NTs with respect to the core–shell material at high bias. In contrast, the enhanced performance of the core–shell samples was attributed to the high electron mobility within the monocrystalline 1D ZnO nanostructure (*i.e.* a five-times lower τ_{dl} value when compared to the bare nanowires due to the efficient separation of charge-carriers at the ZnO@TiO_2 interphase) coupled to the high specific surface area of the TiO_2 polycrystalline shell, which increases the charge-transport about 13% and thus the kinetics for the water photo-electrolysis in this material with respect to the bare ZnO NWs. In conclusion, the efficient application of both the TiO_2 NTs and the ZnO@TiO_2 core–shell photoanodes opens up important perspectives, not only in the water splitting application field, but also for other photo-catalytic applications (*e.g.* photovoltaic cells, degradation of organic substances), due to their chemical stability, easiness of preparation and improved transport properties. Different optimization strategies (*i.e.* co-catalysis, surface modifications to adsorb visible light, increase of thickness, use of concentrated solar light) were identified for each of the studied materials in order to increase their effectiveness and to achieve the efficiency values required for commercial applications.

Acknowledgements

The financial support from the European Commission on the 7th Framework Program NMP-2012 Project Eco$^2CO_2$ (nr.309701) and FCH- JU Call 2011-1 Project ARTIPHYCTION (nr.303435) is gratefully acknowledged.

Notes and references

1 A. Fujishima and K. Honda, *Nature*, 1972, **238**, 37–38.
2 A. A. Ismail and D. W. Bahnemann, *Sol. Energy Mater. Sol. Cells*, 2014, **128**, 85–101.
3 J. R. McKone, N. S. Lewis and H. B. Gray, *Chem. Mater.*, 2013, **26**, 407–414.
4 A. L. Linsebigler, G. Lu and J. T. Yates, *Chem. Rev.*, 1995, **95**, 735–758.

5 M. Gratzel, *Nature*, 2001, **414**, 338–344.

6 C. Bauer, G. Boschloo, E. Mukhtar and A. Hagfeldt, *J. Phys. Chem. B*, 2001, **105**, 5585–5588.

7 D. Fattakhova-Rohlfing, A. Zaleska and T. Bein, *Chem. Rev.*, 2014, **114**, 9487–9558.

8 C. Xiaobo and S. M. Samuel, *Chem. Rev.*, 2007, **107**, 2891–2959.

9 T. P. Chou, Q. Zhang and G. Cao, *J. Phys. Chem. C*, 2007, **111**, 18804–18811.

10 T. Zhao, Y. Zhao and L. Jiang, *Philos. Trans. R. Soc., A*, 2013, **371**, 20130263.

11 A. Wolcott and J. Z. Zhang, *On Solar Hydrogen & Nanotechnology*, John Wiley & Sons, Ltd, 2010, ch. 15, pp. 459–505, DOI: 10.1002/9780470823996.

12 G. Wang, Y. Ling, H. Wang, L. Xihong and Y. Li, *J. Photochem. Photobiol., C*, 2014, **19**, 35–51.

13 C. Xu, Y. Song, L. Lu, C. Cheng, D. Liu, X. Fang, X. Chen, X. Zhu and D. Li, *Nanoscale Res. Lett.*, 2013, **8**, 391.

14 D. Hidalgo, R. Messina, A. Sacco, D. Manfredi, S. Vankova, E. Garrone, G. Saracco and S. Hernández, *Int. J. Hydrogen Energy*, 2014, **39**, 21512–21522.

15 A. Lamberti, A. Sacco, S. Bianco, D. Manfredi, M. Armandi, M. Quaglio, E. Tresso and C. F. Pirri, *Sol. Energy*, 2013, **95**, 90–98.

16 A. Lamberti, A. Sacco, S. Bianco, D. Manfredi, F. Cappelluti, S. Hernandez, M. Quaglio and C. F. Pirri, *Phys. Chem. Chem. Phys.*, 2013, **15**, 2596–2602.

17 V. Farías Rivera, F. Auras, P. Motto, S. Stassi, G. Canavese, E. Celasco, T. Bein, B. Onida and V. Cauda, *Chem. – Eur. J.*, 2013, **19**, 14665–14674.

18 S. Hernández, V. Cauda, A. Chiodoni, S. Dallorto, A. Sacco, D. Hidalgo, E. Celasco and C. F. Pirri, *ACS Appl. Mater. Interfaces*, 2014, **6**, 12153–12167.

19 S. Hernández, V. Cauda, D. Hidalgo, V. Farías Rivera, D. Manfredi, A. Chiodoni and F. C. Pirri, *J. Alloys Compd.*, 2014, **615**, S530–S537.

20 D. Chen, H. Zhang, S. Hu and J. Li, *J. Phys. Chem. C*, 2007, **112**, 117–122.

21 C. Cheng, A. Amini, C. Zhu, Z. Xu, H. Song and N. Wang, *Sci. Rep.*, 2014, **4**, 4181.

22 J. J. Kelly, Z. Hens, D. Vanmaekelbergh and Z. Hensalso, *Encyclopedia of Electrochemistry*, Wiley-VCH Verlag GmbH & Co. KGaA, 2007, DOI: 10.1002/9783527610426.bard060201.

23 Z. Zhang and P. Wang, *Energy Environ. Sci.*, 2012, **5**, 6506–6512.

24 A. Lamberti, A. Sacco, D. Hidalgo, S. Bianco, D. Manfredi, M. Quaglio, E. Tresso and C. F. Pirri, *Acta Phys. Pol., A*, 2013, **123**, 376.

25 X. Yang, A. Wolcott, G. Wang, A. Sobo, R. C. Fitzmorris, F. Qian, J. Z. Zhang and Y. Li, *Nano Lett.*, 2009, **9**, 2331–2336.

26 I. A. Ji, M.-J. Park, J.-Y. Jung, M. J. Choi, Y.-W. Lee, J.-H. Lee and J. H. Bang, *Bull. Korean Chem. Soc.*, 2012, **33**, 2201.

27 K.-S. Ahn, Y. Yan, S. Shet, K. Jones, T. Deutsch, J. Turner and M. Al-Jassim, *Appl. Phys. Lett.*, 2008, **93**, 163117.

28 S. Hoang, S. Guo, N. T. Hahn, A. J. Bard and C. B. Mullins, *Nano Lett.*, 2011, **12**, 26–32.

29 Y. Myung, D. M. Jang, T. K. Sung, Y. J. Sohn, G. B. Jung, Y. J. Cho, H. S. Kim and J. Park, *ACS Nano*, 2010, **4**, 3789–3800.

30 G. Wang, X. Yang, F. Qian, J. Z. Zhang and Y. Li, *Nano Lett.*, 2010, **10**, 1088–1092.

31 G. Wang, H. Wang, Y. Ling, Y. Tang, X. Yang, R. C. Fitzmorris, C. Wang, J. Z. Zhang and Y. Li, *Nano Lett.*, 2011, **11**, 3026–3033.

32 K. Rajeshwar, *Encyclopedia of electrochemistry*, 2002.

33 C. Xu, J. Wu, U. V. Desai and D. Gao, *Nano Lett.*, 2012, **12**, 2420–2424.

34 S. Hernández, G. Saracco, A. L. Alexe-Ionescu and G. Barbero, *Electrochim. Acta*, 2014, **144**, 352–360.

35 S. Hernández, M. Tortello, A. Sacco, M. Quaglio, T. Meyer, S. Bianco, G. Saracco, C. F. Pirri and E. Tresso, *Electrochim. Acta*, 2014, **131**, 184–194.

36 J. Newman, P. G. Hoertz, C. A. Bonino and J. A. Trainham, *J. Electrochem. Soc.*, 2012, **159**, A1722–A1729.

37 I. Gonzalez-Valls and M. Lira-Cantu, *Energy Environ. Sci.*, 2009, **2**, 19–34.

38 M.-S. Lee, I.-C. Cheon and Y.-I. Kim, *Bull. Korean Chem. Soc.*, 2003, **24**, 1155–1162.

39 W. H. Leng, P. R. F. Barnes, M. Juozapavicius, B. C. O'Regan and J. R. Durrant, *J. Phys. Chem. Lett.*, 2010, **1**, 967–972.

40 M. Qorbani, N. Naseri, O. Moradlou, R. Azimirad and A. Z. Moshfegh, *Appl. Catal., B*, 2015, **162**, 210–216.

41 I. Mora-Seró, F. Fabregat-Santiago, B. Denier, J. Bisquert, R. Tena-Zaera, J. Elias and C. Lévy-Clément, *Appl. Phys. Lett.*, 2006, **89**, 203117.

42 Y. Lai, J. Gong and C. Lin, *Int. J. Hydrogen Energy*, 2012, **37**, 6438–6446.

43 G. Dai, S. Liu, Y. Liang and T. Luo, *Appl. Surf. Sci.*, 2013, **264**, 157–161.

44 J. Fan, R. Zamani, C. Fábrega, A. Shavel, C. Flox, M. Ibáñez, T. Andreu, A. M. López, J. Arbiol, J. R. Morante and A. Cabot, *J. Phys. D: Appl. Phys.*, 2012, **45**, 415301.

45 X. Yang, A. Wolcott, G. Wang, A. Sobo, R. C. Fitzmorris, F. Qian, J. Z. Zhang and Y. Li, *Nano Lett.*, 2009, **9**, 2331–2336.

46 Y. Sun, G. Wang and K. Yan, *Int. J. Hydrogen Energy*, 2011, **36**, 15502–15508.

47 J. Gong, Y. Lai and C. Lin, *Electrochim. Acta*, 2010, **55**, 4776–4782.

48 Z. Zhang, M. F. Hossain and T. Takahashi, *Int. J. Hydrogen Energy*, 2010, **35**, 8528–8535.

49 S. Choudhary, S. Upadhyay, P. Kumar, N. Singh, V. R. Satsangi, R. Shrivastav and S. Dass, *Int. J. Hydrogen Energy*, 2012, **37**, 18713–18730.

50 K. R. Reyes-Gil and D. B. Robinson, *ACS Appl. Mater. Interfaces*, 2013, **5**, 12400–12410.

51 J. H. Park, S. Kim and A. J. Bard, *Nano Lett.*, 2005, **6**, 24–28.

52 S. K. Mohapatra, M. Misra, V. K. Mahajan and K. S. Raja, *J. Phys. Chem. C*, 2007, **111**, 8677–8685.

53 Y. Li, Z. Liu, Y. Wang, Z. Liu, J. Han and J. Ya, *Int. J. Hydrogen Energy*, 2012, **37**, 15029–15037.